AGU PUBLICATIONS

JGR

Journal of Geophysical Research: Space Physics

RESEARCH ARTICLE

10.1002/2014JA020511

Key Points:
- New electrostatic 1-D/2-D/3-D model developed to study direct plasma-surface interaction
- The model was used to study plasma above various 2-D lunar surfaces
- Landscape shape dominates properties of plasma above the surface, electric field, and dust

Correspondence to:
S. Dyadechkin,
sergey.dyadechkin@aalto.fi

Citation:
Dyadechkin, S., E. Kallio, and P. Wurz (2015), New fully kinetic model for the study of electric potential, plasma, and dust above lunar landscapes, *J. Geophys. Res. Space Physics*, *120*, 1589–1606, doi:10.1002/2014JA020511.

Received 21 AUG 2014
Accepted 28 JAN 2015
Accepted article online 5 FEB 2015
Published online 4 MAR 2015

New fully kinetic model for the study of electric potential, plasma, and dust above lunar landscapes

S. Dyadechkin[1], E. Kallio[1], and P. Wurz[2]

[1]School of Electrical Engineering, Aalto University, Espoo, Finland, [2]Physics Institute, University of Bern, Bern, Switzerland

Abstract We have developed a new fully kinetic electrostatic simulation, HYBes, to study how the lunar landscape affects the electric potential and plasma distributions near the surface and the properties of lifted dust. The model embodies new techniques that can be used in various types of physical environments and situations. We demonstrate the applicability of the new model in a situation involving three charged particle species, which are solar wind electrons and protons, and lunar photoelectrons. Properties of dust are studied with test particle simulations by using the electric fields derived from the HYBes model. Simulations show the high importance of the plasma and the electric potential near the surface. For comparison, the electric potential gradients near the landscapes with feature sizes of the order of the Debye length are much larger than those near a flat surface at different solar zenith angles. Furthermore, dust test particle simulations indicate that the landscape relief influences the dust location over the surface. The study suggests that the local landscape has to be taken into account when the distributions of plasma and dust above lunar surface are studied. The HYBes model can be applied not only at the Moon but also on a wide range of airless planetary objects such as Mercury, other planetary moons, asteroids, and nonactive comets.

1. Introduction

The Moon interacts directly with its space environment due to the absence of any atmosphere and thus does not possess an ionosphere like Earth, Venus, and Mars. The Moon does not have either any global intrinsic magnetic field, contrary to Earth, Mercury, and the giant planets.

The direct plasma-surface interaction makes the Moon an ideal object for understanding various physical processes near the surface, which are expected to take place in many atmosphere-less objects, like asteroids and other planetary moons in the solar system, the Martian moons Phobos and Deimos, the Jovian moons, and many others. The plasma above the lunar surface contains solar wind particles (protons and electrons) and charged particles originating from the surface (photoelectrons); on the dayside, mainly photoions are present but also electrically charged dust particles. The direct plasma-surface interaction results in a charged plasma sheath above the surface, the Debye layer, and associated electric potential and electric fields within the layer. The electric field enables charged particles, such as dust particles to be levitated and transported over the surface. The physics within the Debye layer is an interesting topic, because the plasma properties are affected by many factors [*Kallio et al.*, 2012]: (1) the plasma properties of the solar wind protons and electrons, (2) secondary particles (electrons, positively and negatively charged ions) from the surface resulting from the impact of solar wind particles on the surface, (3) photoelectrons from the surface at places exposed to sunlight, (4) charged dust particles above the surface, which are also sinks and sources for ions and electrons, (5) the interplanetary magnetic field (IMF) or the magnetic field associated with the Earth's magnetosheath or in the magnetosphere, (6) possible local magnetic anomalies, (7) the convective electric field associated with the flow of the solar wind or the electric field in the Earth's magnetosheath or in the magnetosphere, [8] the electric field within the Debye sheath, (8) the EUV light which has variations due to the temporal variations of the Sun and due to the orbital motion of the Moon around the Earth, (9) physical and chemical properties of the surface, which is the source of charged particles, and (10) the three-dimensional shape of the surface, such as mountains and craters. In the solar wind, the nominal Debye length is few meters, and it is even smaller near the lunar surface due to photoelectrons. Therefore, many interesting plasma processes take place within a few meters above the lunar surface.

One of the most important reasons to develop a model that describes the electric field and the properties of plasma and dust near the lunar surface originates from the Surveyor and Apollo missions in the 1960s and the 1970s. Especially, photographs taken at those missions showed a horizontal glow that was interpreted to be caused by light scattered from dust elevated above the lunar surface [see, e.g., *Criswell*, 1973; *Rennilson and Criswell*, 1974; *Zook and McCoy*, 1991, and references therein]. A possible mechanism to accelerate and transport dust particles at the Moon, and other Moon-like planetary bodies, was suggested to be electric fields near the surface [see, e.g., *Criswell*, 1973; *Walker*, 1973, and also references therein].

Historically, the one-dimensional (1-D) electric potential associated with pure photoelectron situation for certain specific velocity distribution functions has been successfully derived analytically [*Grard and Tunaley*, 1971]. Later, a three-component plasma (solar wind electrons and protons, and photoelectrons) obeying a Maxwellian velocity distribution function at a constant temperature was studied using 1-D analyses [*Nitter et al.*, 1992, 1998]. This three-component plasma model suggested that the electric potential within the Debye layer is nonmonotonic and that a local minimum exists in the potential. This local potential minimum has an important implication because the electric field accelerates positively charged dust particles upward below the potential minimum and downward above. In such a potential structure a dust particle can become trapped in the potential minimum and levitate above the surface, as illustrated in 1-D simulations [*Nitter et al.*, 1998; *Poppe and Horányi*, 2010].

Modern computer simulations have extended the analysis to 2-D cases and to situations with non-Maxwellian velocity distribution function. One-dimensional numeric particle-in-cell (PIC) simulations have shown how the properties of the electric potential depend on the velocity distribution of photoelectrons [*Poppe and Horányi*, 2010], on the solar zenith angle (SZA) [*Poppe*, 2011] and on the temperature of the solar wind and magnetospheric plasma sheet [*Poppe et al.*, 2011, 2012a]. Furthermore, 2-D PIC simulations have stressed how strongly 2-D surface features may affect the near-surface electric potential [*Zimmerman et al.*, 2011; *Poppe et al.*, 2012b].

The previous direct 1-D and 2-D plasma-surface interaction simulations have emphasized the need for a comprehensive generic PIC simulation that can take into account surface features, varying surface properties and various plasma populations, and velocity distribution functions. This paper presents a new fully kinetic electrostatic PIC model, HYBes, aimed at studying properties of plasma above the surface of the Moon and other airless bodies in 1-D, 2-D, and 3-D. The robust new model is tailored to study in a simple manner various surface features such as mountains or craters. Nonplanar surface shapes or reliefs may also be combined to realistically model man-made objects, such as a spacecraft or a Moon base. The model also permits the study of how the different physical properties of the surface may affect the solution, such as conducting/nonconducting or sunlit/shadowed regions or regions with different photoelectron yields.

One major goal for the developed model is to study properties of dust above the lunar surface, that is, the particle density, size and charge distribution, and the velocity distribution. However, it is not well established how dust particles can in the first place become liberated from the surface following the complex interplay between an upward pointing force, which exceeds the gravitational force, and a downward pointing cohesive force between the dust particle and the surface [*Hartzell and Scheeres*, 2011]. Different mechanisms have been proposed that enable the release of dust particles from the surface, such as electrostatic forces, seismic activity, and micrometeoroid bombardment [see, e.g., *Hartzell and Scheeres*, 2011, and references therein]. The role of electrostatic forces has been suggested to be especially important near the day-night terminator region that separates mostly positively charged surface of the sunlit hemisphere and the mostly negatively charged shadowed hemisphere [*Farrell et al.*, 2011]. High electric potentials are also anticipated to be observed near 2-D landscapes when the solar wind flows horizontally above a crater [*Zimmerman et al.*, 2011]. The maximum potential drop within the Debye layer is associated with the temperature of plasma electrons and, therefore, electrostatic forces can be enhanced when the Moon is under the influence of a hot ambient plasma associated with solar storms or, occasionally, when the Moon is within the Earth's plasma sheet [*Poppe*, 2011].

In this paper HYBes has been used to study how the landscape morphology affects the properties of dust above the surface once dust particles are lifted from the surface. The response of four natural landscape features and of a landscape that mimics a man-made structure (a Moon base) to dust densities is compared

with a flat surface case by keeping the charge of the dust particle unchanged and treating dust particles as test particles. As shown later in the paper, the landscape affects strongly the 2-D electric potential and, consequently, the distribution of lifted dust above the surface.

The paper is organized as follows. First, properties of the new model developed are described in detail. Special emphasis is put on describing challenges associated with the boundary conditions and how the simulation takes into account the different physical properties of the surface. Second, the applicability of the model is demonstrated by deriving 1-D potential and electron density profiles for different Solar Zenith Angles (SZA). The main morphological situations applied here are six landscape features where 2-D electric potentials are derived. Subsequently, the obtained electric potentials are used to study how the landscapes affect the spatial distribution of dust for two scenarios: (1) a homogeneous dust emission for the surface and (2) for a dust point source on the lunar surface at various places.

2. Basics of the HYBes Model

The Cartesian grid structure and the macroparticle accumulation used in the HYBes are similar to those of the HYB model that has been used in the 3-D hybrid model simulations [see *Dyadechkin et al.*, 2013].

The HYBes model is a full particle-in-cell (PIC) model where both ions and electrons are modeled as particles. The model uses the Cartesian staggered grid with rectangular outer boundaries as a simulation domain. The staggered grid means that different variables are placed on different grid elements. The simulation mesh consists of the cubic-shaped cells, and each cell, in turn, consists of six faces (which contain average values over the face area) and a cell center (which contains the volume average value). Each cell is connected by its faces with six neighboring cells. The simulation domain is limited by six outer edges called "walls": $+X$ and $-X$ walls, which are referred to in this paper as the front and back walls, respectively, and the $+Y$, $-Y$, $-Z$, and $+Z$ walls are referred to as the side walls.

The scalar field quantity in the simulation, the electric potential, is evaluated at the cell centers, and the vector field quantities, the electric field and the time-independent magnetic field, are stored on the cell faces and in the cell centers, respectively.

In the HYBes model the particles are represented by macroparticle clouds. A macroparticle, j, is characterized by the statistical weight (w_j), which represents the number of real particles with mass m_j and electric charge q_j. In the HYBes model the weight can vary between different macroparticles. A macroparticle is moved and accelerated like a single particle under the Lorentz force and gravitation. The macroparticles in the HYBes model have a finite size, equal to the grid cell size. A macroparticle can be described as a cloud of cubic shape with a uniform distribution of charge and mass. When such a macroparticle j moves, it represents the motion of w_j ions or electrons, each of them having the same speed as the macroparticle. The electric charge, mass, and momentum of a macroparticle is accumulated into the grid by calculating the geometrical intersection between the macroparticle and grid cells. On the 3-D mesh the contribution of each macroparticle in a specific cell is part of the macroparticle cloud volume located inside the cell.

The HYBes model solves the following equations for particles and fields:

$$\frac{d\mathbf{v}_{e,i}}{dt} = \frac{q_{e,i}}{m_{e,i}}\left(\mathbf{E} + \mathbf{v}_{e,i} \times \mathbf{B}\right) + \frac{\mathbf{F}_{\text{gravitation}}}{m_{e,i}}, \tag{1}$$

$$\frac{d\mathbf{x}_{e,i}}{dt} = \mathbf{v}_{e,i}, \tag{2}$$

$$\mathbf{E} = -\nabla\phi, \tag{3}$$

$$\nabla^2\phi = -\frac{\rho_q}{\epsilon_0}, \tag{4}$$

where subscript e and i denote electrons and ions, respectively.

Equation (1) is Newton's second law including the Lorentz force and gravitational force $F_{\text{gravitation}}$. In equation (1) $m_{e,i}$ and $q_{e,i}$ are the mass and charge of the particles, respectively. Equation (3) defines the electrostatic field $\mathbf{E}$, which is derived from the electric potential ϕ. Equation (4) is the Poisson's equation, where ϕ is the electric potential, ρ_q is the total charge number density, and ϵ_0 is the vacuum permittivity.

The system of HYBes model equations describes the evolution of particle positions in the electrostatic electric field **E** and in the magnetic field **B**. In the electric field the particle positions are calculated self-consistently from their initial state while the magnetic field is assumed to be unchanged during the simulation. The electric field is saved on cell faces and the electric field at the position of a particle is derived from the face electric field by linear interpolation. In the HYBes model the particles are propagated with a leapfrog algorithm and time-reversible second-order accurate Buneman scheme [*Hockney and Eastwood*, 1988, p. 112].

2.1. Solving Poisson's Equation

To get the electrostatic electric field **E** the Poisson equation (4) is solved. In the HYBes model the Poisson's equation can be solved with Jacobi, Gauss-Seidel, or Successive Over Relaxation (SOR) iteration methods [see, e.g., *Jardin*, 2010]. In the results presented in this paper the Jacobi iteration method is used:

$$\phi^{n+1}_{(i_x,i_y,i_z)} = \left(\phi^{n}_{(i_x-1,i_y,i_z)} + \phi^{n}_{(i_x+1,i_y,i_z)} + \phi^{n}_{(i_x,i_y-1,i_z)} + \phi^{n}_{(i_x,i_y+1,i_z)} + \phi^{n}_{(i_x,i_y,i_z+1)} + \phi^{n}_{(i_x,i_y,i_z-1)} + \frac{dl^2 \rho^{n}_{q}}{\epsilon_0} \right) /6, \quad (5)$$

where n is the number of iterations per time step dt. In the runs presented in the paper, the maximum number of iteration was chosen large enough, $n_{\mathrm{Max}} = 50{,}000$, to ensure that the needed accuracy is reached.

The iteration method requires an initial ϕ value, and it is assumed that $\phi^0 = 0$ in the whole simulation domain. The desired accuracy is obtained by continuing the iteration until the relative difference of the solution between the new (ϕ^{n+1}) and the previous (ϕ^n) iteration value at each cell fulfills the criterion

$$\frac{\phi^{n+1} - \phi^n}{\phi^n} < \epsilon_{\mathrm{iteration}}. \quad (6)$$

Here $\epsilon_{\mathrm{iteration}}$ is the required accuracy, which is defined in the beginning of the simulation. In the runs presented $\epsilon_{\mathrm{iteration}}$ was set to 10^{-8}. The maximum number of iterations is limited by n_{Max} if the required accuracy was not reached.

2.2. Boundary Conditions

The characteristic feature of a PIC simulation is that it is computationally expensive and that the computational costs are decreased by simulating only a small region of space covering the global interaction region, for example, the solar wind interacting with the lunar surface. There are numerous standard solvers for Poisson's equation that can be used to derive electric potential from a given charge density distribution, but the boundary conditions are often tailored for the analyzed specific problem. Therefore, the applicability and realism of the used PIC simulation depends critically on the used boundary conditions (BCs). The goal of this chapter is to present in detail the developed new boundary conditions and to discuss the rationale behind the choices and developed methods.

2.2.1. Boundary Conditions: Electric Potential

The boundary conditions (BCs) are set up on the extra layers located outside of the simulation region. These so called "ghost cells" have the same characteristics as the internal simulation cells, but they do not contain macroparticles. Therefore, quantities derived via the accumulation process within the simulation domain can be brought in the ghost cells only by applying boundary conditions.

The Neumann BCs are used at the boundary for the electric potential in this study. The Neumann BC specifies the derivatives of the solution on the boundaries of the simulation domain. These derivatives are set to zero to implement the free outflow of the plasma and electric field from the simulation. Technically speaking, in the Neumann BC the cell-centered value of the ρ_q is copied from the outermost cells of the simulation box to the ghost cells.

The Jacobi iteration method (equation (5)) requires to set up the BC for the electric potential ϕ on the front wall, the back wall, and the side walls of the simulation box.

For all simulations presented in this paper we assume that components of electric field perpendicular to the side walls are zero, that is, $E_y = 0$ at $y = $ const. walls and $E_z = 0$ at $z = $ const. faces. Therefore, for the side walls, the potential values are copied from the outermost cells of the simulation box to the ghost cells. Boundary conditions for the electric potential on the front and back walls are derived from the surface average electric fields, that are described in detail in Appendix A.

2.2.2. Boundary Conditions: Magnetic Field

An arbitrarily oriented constant magnetic field can be set up, which will be a constant during the simulation. The magnetic field is inserted into the center of each grid cell initially or as a constant magnetic field term (B_0) added in equation (1).

2.2.3. Boundary Conditions: Particles

The HYBes supports three different boundary conditions: absorbing, reflecting, and periodic. In the absorbing BC, a particle is removed from the simulation box if it crosses the boundary. The reflecting BC returns the particle to the simulation box so that the perpendicular (to the boundary) component of the velocity of the particle is reversed. The periodic BC also returns the particles to the simulation box so that if a particle reaches the outer boundary at, for instance, the $+Y$ wall, it is moved to the opposite boundary, the $-Y$ wall, keeping the velocity unchanged. The particle BC at the boundary can be specified for each particle population (for each type of ions and electrons) separately. The particle BC is also used to enter a plasma into the simulation box. For this reason the macroparticles are generated with random positions in the front cells of the simulation walls. The macroparticles in the incident flow are generated with random positions on the inflow wall and random velocities, assuming that the entering plasma flow is characterized by a number density and by thermal and bulk velocities.

In the results presented in this paper we treat the lunar surface as an insulating surface. It means that if a particle hits the surface it is accumulated in the first cell layer under the lunar surface, which is also a part of the simulation box. After that the particle position is not changed during the simulation time, but its electric charge contributes to the total charge number density and, consequently, to the electric potential.

Another highly important boundary condition is the boundary condition for particles at the solar wind wall, i.e., at the front wall (the $+X$ wall). First of all, if a particle hits the front wall it is removed from the simulation. The most critical boundary condition controls how the solar wind particles are injected into the simulation box to obtain a stationary solution where the electric field on the front face is zero. This is ensured by the so-called density regulator, DR, which controls the density of the solar wind electrons that are injected into the solar wind by monitoring the total electric charge within the simulation box, Q. The DR increases or decreases the density of injected solar wind electrons if Q is positive or negative, respectively. In such a way Q becomes closer to zero within the simulation box and, consequently, also the electric field near the front wall becomes closer to zero (see equation (A3)). In the presented runs the average total charge were calculated during 2×10^{-3} s and the density of the solar wind electrons was increased or decreased by 0.5% if Q was positive or negative, respectively. The motivation and rationale of the developed DR method is described in Appendix B.

2.3. Macroparticle Propagation and Accumulation

One of the crucial points of the HYBes model is the accumulation of mass and charge of the macroparticles in the grid cells. In our model the shape and size of a macroparticle coincides with the local shape and size of the grid cells and, as already mentioned, the accumulation process is just a geometrical intersection of a macroparticle with the simulation lattice. If, for instance, such a macroparticle moves from the position 1 to position 2, the total mass, electric charge, momentum, and kinetic energy in the accumulation process over all grid cells remain unchanged and are conserved.

There are several types of macroparticle populations in the HYBes model: the Moon population, the solar wind populations, and the dust populations. The Moon population includes photoelectrons, which are emitted from the lunar surface, and the rate of emission is defined by the solar photon flux. The solar wind populations include solar wind protons and solar wind electrons. All these particles are injected in the simulation box from the front wall. The dust particle populations include lunar dust particles, and they are injected into the simulation box as well as the photoelectrons, from the back wall of the simulation domain.

All macroparticles are injected in the simulation box with certain bulk velocity, thermal velocity, the macroparticle weight w, mass m, and charge q. The rate of emission for each type of population is defined by the different criteria and will be described in detail below in section 3.

2.4. Cell Structure and the Material Index

The HYBes model uses the rectangular simulation domain, which consists of a number of cells. An important technique in the model is that physical properties of an individual cell can be controlled in a flexible manner.

0	0	0	0	0	0	0	0	0	0	0	0	0	0
0	0	0	0	0	0	0	0	0	0	0	0	0	0
0	0	0	0	0	0	0	0	0	0	0	0	0	0
0	0	0	0	0	0	0	0	0	0	0	0	0	0
0	0	0	0	1	1	1	1	1	1	0	0	0	0
0	0	0	0	2	3	3	3	3	2	0	0	0	0
0	0	0	0	2	2	3	3	2	2	0	0	0	0
0	0	0	0	0	2	3	3	2	0	0	0	0	0
0	0	0	0	0	2	3	3	2	0	0	0	0	0
1	1	1	1	2	2	3	3	2	2	1	1	1	1
3	3	3	3	3	3	3	3	3	3	3	3	3	3
3	3	3	3	3	3	3	3	3	3	3	3	3	3
3	3	3	3	3	3	3	3	3	3	3	3	3	3

Figure 1. Illustration of the material index in the HYBes model in the analyzed Moon base type of landscape. All cells have an index, the material index, which determines how a cell treats a particle which hits against the cell. Cells with the material index 0 are cells above the surface and cells with the material indexes 1, 2, and 3 are surface cells. Some of the surface cells can emit photoelectrons (material index 1), some only absorb particles (material index 2), and some cells deep inside the material cannot emit, absorb, or keep charged particles inside the cell (material index 3). See text for details.

Each cell has some specific number, so-called material index, which regulates the physical properties of the cell, including how the cell treats particles. Figure 1 shows an example of the simulation domain in the 2-D model for the Moon base case. For this particular case we use four different material indices:

1. *Cells with the material index 0: "Space" cells*. If a cell has a material index *0* the macroparticles can freely move inside the cell under the influence of the existing forces. Those are cells above the surface.
2. *Cells with the material index 1: "Emitting" cells*. If a cell has a material index *1* macroparticles are emitted from the faces of the cell. The faces which emit the macroparticles should touch the "space" cells. The "emitting" cells can also absorb a macroparticle if the particle hits the cell face. An example of this type of cell is a cell on the surface which emits photoelectrons.
3. *Cells with the material index 2: "Absorbing" cells*. If a cell has a material index *2* macroparticles are absorbed by the cell. If the particle hits the face of such cell, it is stored at the cell center. Therefore, the electric charge and the mass of the cubic macroparticle cloud are totally accumulated inside this cell without any contribution to the neighbors. The difference between the cell with material indices *1* and *2* is that the cell with material index *1* can emit and absorb macroparticles, while the cell with material index *2* can only absorb them. An example of this type of cell is a cell on the surface in a shadow, which does not emit any particles from the surface.
4. *Cells with the material index 3. "Inner" cells*. If a cell has a material index *3* the macroparticles cannot move inside such a cell. If after one time step d*t*, particles have moved inside such an "inner" cell, its position is returned to the closest cell with material index *1* or *2*. These cells are inside the lunar surface and in the simulation mesh they are situated below cells which have material indices 1 or 2 (cf. Figure 1).

Note that by using this material index structure, we can build any type of surface landscape that consists of cubic-shaped cells. The index provides also a possibility to implement easily different boundary conditions. For example, a conducting surface model can be obtained by using a constant electric potential value at all material indexes 1–3 when the Poisson equation is solved. The material index method is very flexible because it allows us to specify new types of cells with different physical properties.

3. Simulation Results

In this section the developed model is used to study a plasma consisting of three charged particle populations, including solar wind protons, solar wind electrons, and lunar photoelectrons. Furthermore, this solution was used to study dust particles as test particles.

In the runs presented in this section the Moon is assumed to be in a nominal solar wind plasma where the density of the undisturbed solar wind protons were $n_{sw}(H^+) = 10$ cm^{-3}, the bulk velocity is $U_{sw}(H^+) = 400$ km s^{-1}, and the kinetic temperature $T_{sw}(H^+) = 10$ eV. The bulk velocity of the solar wind electrons was also set to $U_{sw}(e^-) = 400$ km s^{-1}. The thermal velocity of electrons, $U_{sw,therm}(e^-)$ $(=\sqrt{k_B T_{e^-}/m_e})$, was 1.36×10^3 km s^{-1}, which corresponds to temperatures of about $k_B T_{e^-} = 10.5$ eV. Consequently, the Debye length, λ_D, in the undisturbed solar wind was therefore 7.6 m ($\lambda_D = \sqrt{(\epsilon_0 k_B T(e^-))/(n(e^-)e^2)} \sim 69\sqrt{(T(e^-)[\mathrm{K}])/(n(e^-)[\mathrm{m}^{-3}])}$ m where k_B is the Boltzmann constant, $n(e^-)$ is the density of electrons,

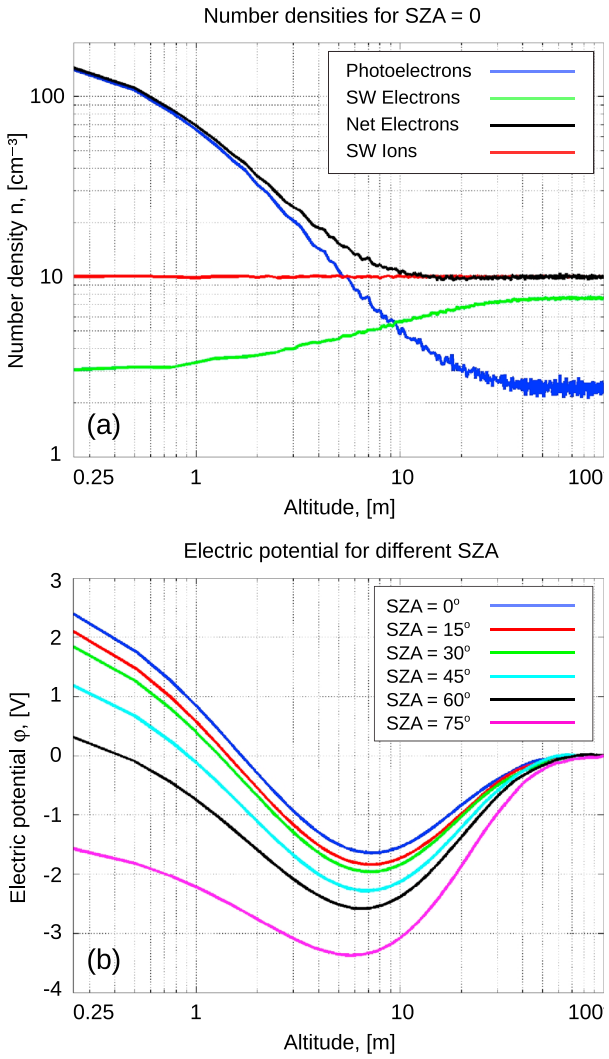

Figure 2. (a) The particle density of the three-particle populations in the HYBes simulation and the total electron density. (b) The electric potential at different SZA values. The simulation was performed by 1-D HYBes model.

and $T(e^-)$ the temperature of electrons). The velocity distribution function of the solar wind protons and electrons was assumed to be a 3-D Maxwellian velocity distribution function.

Photoelectrons were modeled by a 3-D Maxwellian velocity distribution function with the thermal velocity of 621 km s^{-1}, which corresponds to a temperature of about $k_B T_{e^-} = 2.2$ eV, and the photoelectron emission current density at the subsolar point was assumed to be 4.5 μA m^{-2}, as used in previous 1-D PIC simulations [see, e.g., *Poppe and Horányi*, 2010]. In addition, electrons above 6 eV were removed from the velocity distribution because a Maxwellian velocity distribution produces a high-energy tail, whereas the energy of the emitted photoelectron is limited by the energy of the absorbed solar photon.

The density of dust is derived by using the HYBes model in its test particle mode when the electric potential is kept constant during the run. This has to be done because the time it takes to obtain a relatively stationary dust density distribution is substantially larger than a typical simulation time in the HYBes PIC simulation, as will be discussed in detail later in section 3.3. For example, the dust density profiles shown in this paper are derived at $t = 50$ s after the start of the continuous dust emission, while the shown stationary 2-D PIC simulations are obtained at $t = 1$ ms. The velocity distribution function of the emitted dust particles is not known, and in the dust simulations presented in this paper the velocity distribution function was assumed to be a 3-D Maxwellian with the bulk velocity of 10 m s^{-1} and the thermal velocity of 10 m s^{-1}. The emitted dust particles are assumed to have identical physical properties. The mass of a dust particle was assumed to be $m_{\text{dust}} = 8.89 \times 10^{-19}$ kg ($\sim 5.3 \times 10^8\ m_p$) and the electric charge of the dust particle, $q_{\text{dust}} = +1.672 \times 10^{-17}$ C ($\sim$105 e). For comparison, if we assume that a dust particle is a homogeneous spherical ball with a mass density of $\rho_m = 1.5$ g cm^{-3}, the radius of the dust particles would be about $r \approx 0.05$ μm ($m_{\text{dust}} = \rho_m \frac{4}{3}\pi r^3$). Moreover, the electric charge of a spherical dust particle corresponds to a dust potential of about $V_{\text{dust}} \approx 3$ V ($q_{\text{dust}} = V_{\text{dust}}\, 4\pi\epsilon_0 r$).

It is also not known how dust particles can be lifted from the lunar surface and at which locations. Therefore, two dust emission modes have been used in this study: (1) a homogeneous emission model where the flux of emitted dust particle per horizontal area (i.e., per upward pointing face of a simulation cell on the surface) was constant and (2) a point source model where dust particles were emitted only at a single simulation cell face from the surface. The size of the 1-D PIC simulation box was 0 m $< x <$ 100 m and -0.125 m $< y, z <$ 0.125 m, $dl = 0.25$ m and in the 2-D HYBes simulation 0 m $< x <$ 100 m, -40 m $< y <$ 40 m and -0.25 m $< z <$ 0.25 m, $dl = 0.5$ m. The number of grid cells without ghost cells in the 1-D case was $n_x \times n_y \times n_z = 400 \times 1 \times 1$ and in the 2-D case $200 \times 160 \times 1$. The simulation time step was 5.0×10^{-8} s. The simulation time step was chosen to be so small that the majority of electrons do not jump over a cell during

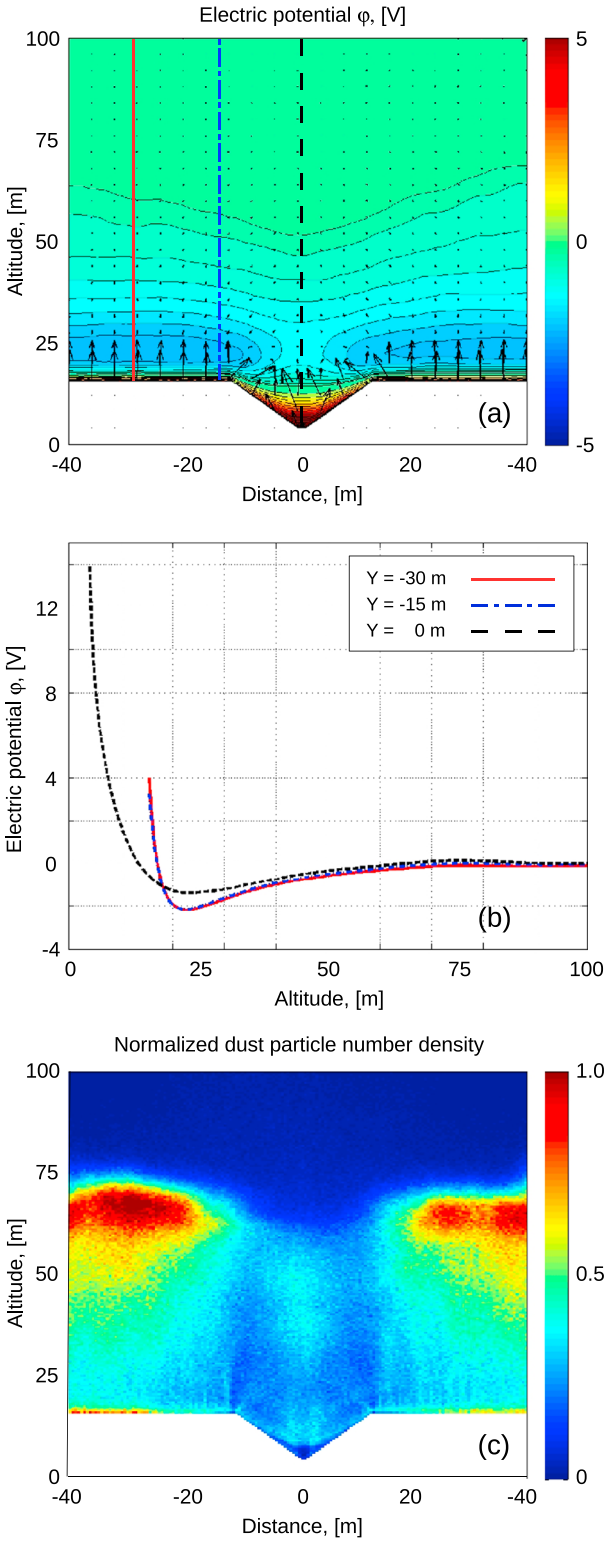

Figure 3. (a) The electric potential above the lunar surface for the antipyramid landscape. The vectors show the corresponding electric field. (b) Electric potential along the three vertical lines indicated in Figure 3a. (c) Normalized density of monosized dust particles that are emitted uniformly from the surface. The simulation was performed using the 2-D HYBes model.

the time step (0.25 m/5 × 10^{-8} s = 5000 km/s; 0.5 m/5 × 10^{-8} s = 10,000 km/s; thermal velocity of solar wind electrons: 1360 km/s). Typical number of macroparticles was about (1–5) · 10^6 depending on simulations.

3.1. Debye Layer in 1-D

The Debye layer based on the 1-D HYBes simulation is illustrated in Figure 2, which gives the particle densities and the total density of electrons above the Moon surface. Note that the density of solar wind protons is practically constant at all altitudes because the change of the energy of protons within the Debye sheath is small compared to their initial energies. Near the surface, almost all electrons are photoelectrons but the solar-wind electrons start dominating the electron population at higher altitudes near the front wall. As in the previous 1-D PIC simulations [*Poppe and Horányi*, 2010], the total density of electrons exceeds, or is very close to, the density of protons and, therefore, the total charge above the surface is negative. Note also that the density of the solar wind electrons at the front face is about 7.5 cm^{-3}, that is, about 75% of the density of the solar wind protons, and the quasi-neutrality at the front wall is obtained because of the about 25% density contribution of photoelectrons.

Figure 2b shows the electric potential at different SZA values. The SZA effect was modeled by reducing the vertical velocity of the solar wind protons by taking into account the cosine dependency of the SZA: $U_{sw}(H^+)(\mathrm{SZA}) = \cos(\mathrm{SZA}) \times U_{sw}(H^+)$. The cosine dependency was also taken into account in the photoelectron flux, which was cos(SZA) × 4.5μA m^{-2}. In the plot the potential is normalized to be zero at the front wall. Characteristic features of the solutions are that increasing SZA results in smaller potential values and that the local potential minimum moves closer to the surface, in a similar way as in the previous 1-D PIC simulations [e.g., *Poppe*, 2011]. Note also that the nonconstant electric potential near the surface implies that the electric field is nonzero there and that it points upward near the surface, because the surface is positively charged while the sum of the electric charges collected above the surface is negative.

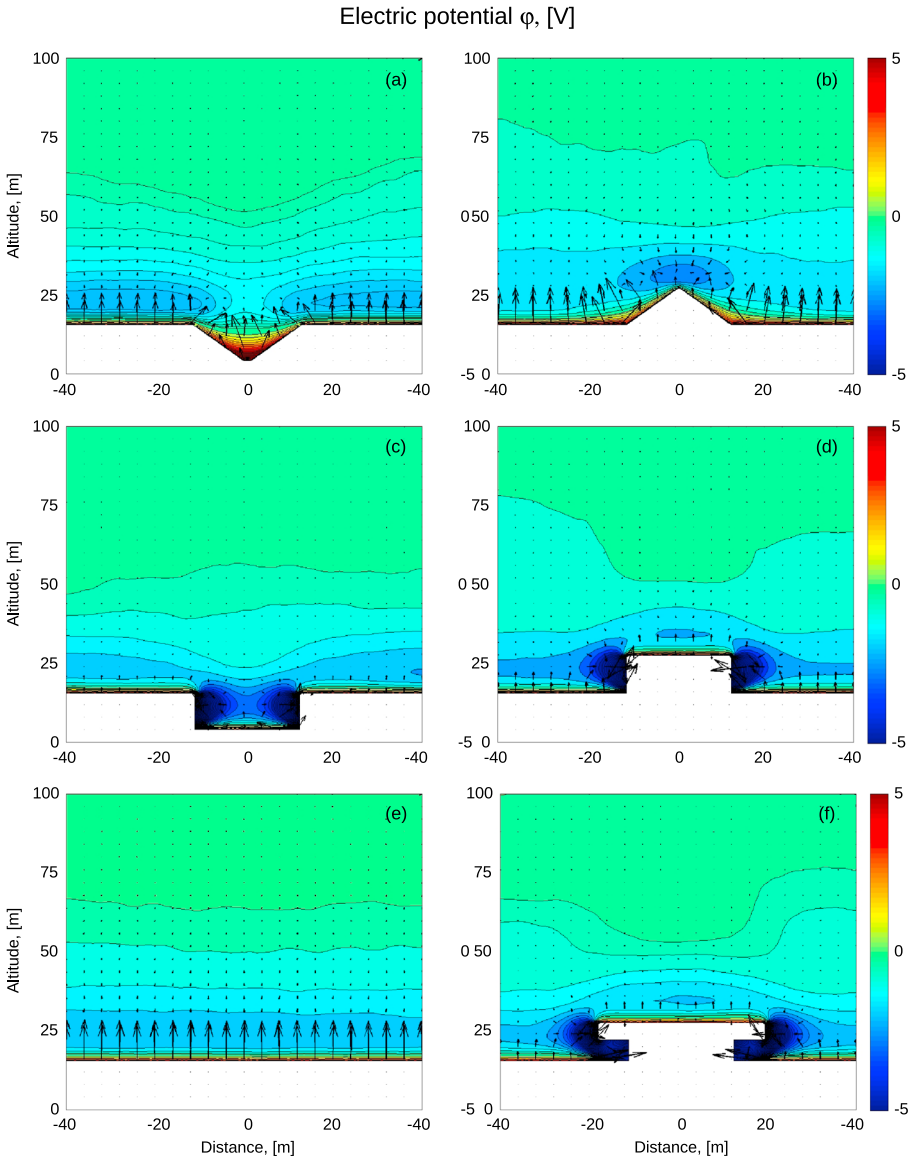

Figure 4. The electric potentials for the six landscapes analyzed by the HYBes model: (1) the pyramid (this case is identical to the case illustrated in Figures 3a and 3b), (2) the antipyramid, (3) the crater, (4) the mountain, (5) the flat surface (this panel, to some extent, represents the result of 1-D simulation (Figure 2a blue line)), and (6) the Moon base. The vectors are electric field vectors. The simulation was performed using the 2-D HYBes model.

3.2. Debye Layer in 2-D

The 2-D HYBes was used to study Debye sheath regions for six different surfaces, i.e., for the so-called (1) flat surface, (2) pyramid, (3) antipyramid, (4) mountain, (5) crater, and (6) Moon base surface reliefs. All cases are modeled for SZA = 0°. The flat surface mimics the situation where the length scale of the landscape (L) was much larger than the Debye length (λ_D), that is, when $L \gg \lambda_D$. The other landscape cases were used to study the role of the Debye sheath. Therefore, their sizes were chosen to be comparable with the Debye layer, i.e., the size scale of $L \sim \lambda_D$. Figure 3 shows the key parameters in the antipyramid surface case. The electric field points upward at every location on the surface and it is strongest at the deepest point of the antipyramid. Three vertical lines show the position where the 1-D electric potential cuts are derived and analyzed in Figure 3b. Note that the electric potentials above the surface at $y = -30$ m and $y = -15$ m are quite similar to those obtained for the 1-D case at SZA = 0°. However, the electric potential above the center of the antipyramid ($y = 0$ m) is much larger than those at the two other analyzed locations. Note also that all three potential curves have a local minimum above the surface and, consequently, that the electric

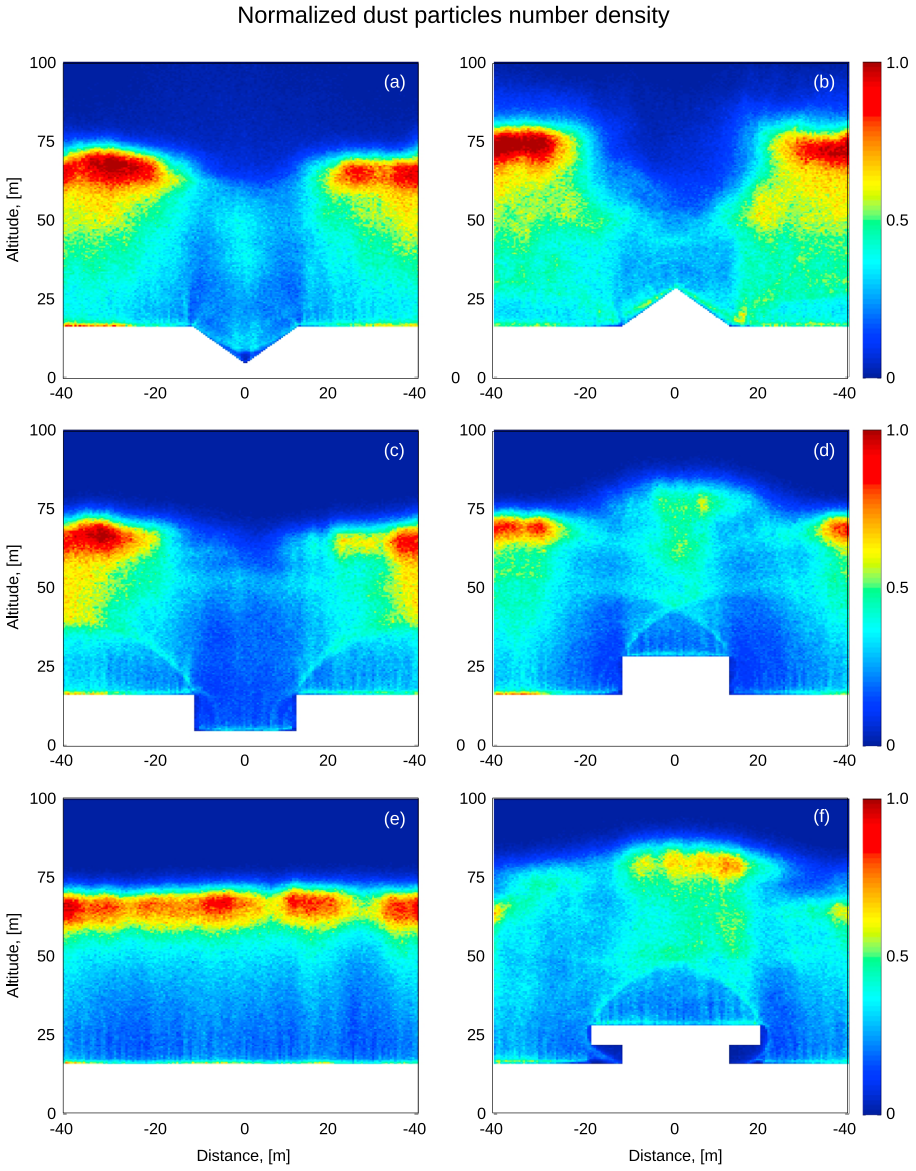

Figure 5. The distribution of homogeneously emitted dust above six analyzed landscapes. See Figure 4 for the corresponding electric potential and electric field structures. All panels are normalized by the same maximum density value. Note that densities contain temporal nonsymmetric features due to statistical fluctuations. The simulation was performed using the 2-D HYBes model.

field points upward below the potential minimum point and downward above it. In Figure 3c the density distribution of dust was derived by using the electric potential shown in Figure 3a and by using a homogeneous dust emission model. The dust emission flux from the surface is not known and, therefore, Figure 3c shows the dust densities divided by the maximum dust density. It should be noted, that the normalized dust densities also give an indication about the probability for a single dust particle to occupy a given location in the following manner: If there is a dust particle in the cell where the normalized density is 1, then the values of the normalized density at other cells give the probability to find a dust particle at those cells. The dust density shows that a local dust maximum exists at about 65 m above the surface where the surface is flat. At that altitude the upward motion of many dust particles changes to a downward motion and the associated velocity decrease can be seen as increased density. Note that the dust particles emitted from inside the antipyramid get a high upward directed acceleration due to the large electric field. They are also accelerated horizontally by the horizontal component of the electric field near the antipyramid (see electric field vectors in Figure 3a) resulting in low-density regions above the antipyramid.

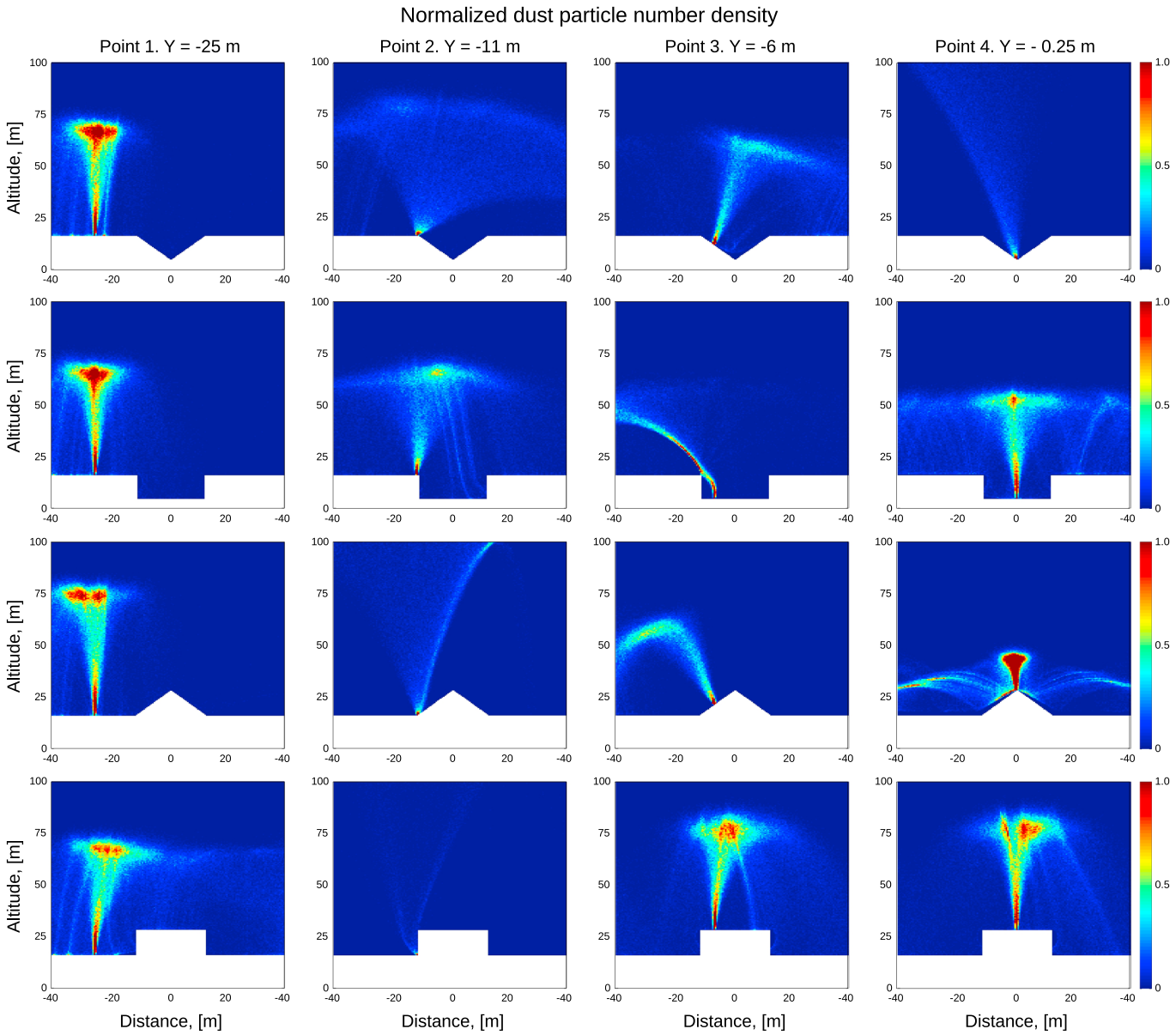

Figure 6. The normalized density of dust above four different landscapes when dust is emitted from a surface at various points. The rows from top to bottom represent the antipyramid case, the crater case, the pyramid case, and the mountain case. Four columns from left to right show densities that resulted from four source points on the surface at $y = -25$ m, $y = -11$ m, $y = -6$ m, and $y = -0.25$ m, respectively. See Figure 4 for the corresponding electric potential and electric field structures. All panels are normalized by the same maximum density value. The simulation was performed using the 2-D HYBes model.

The summary of the electric potential at six landscape dust simulations can be seen in Figure 4. Every landscape results in its own type of electric potential structure. In the pyramid landscape (Figure 4b) the global potential minimum is located above the top of the pyramid. On the crater (Figure 4c) and on the mountain (Figure 4d) landscapes, the global potential minimum is situated near the places where the surface has vertical surfaces. The low-potential regions are formed where electrons can easily hit into the vertical surfaces because of their high thermal velocity compared with the bulk velocity (electrons are subsonic), while the protons form a beam-like downward moving flow (solar wind protons are highly supersonic). Moreover, vertical faces do not emit photoelectrons at the SZA = 0° and, therefore, the photoelectron emission does not make those surfaces positively charged. Both of these effects make vertical surfaces more negatively charged compared with the horizontal surface on the flat surface (Figure 4e) case. The most negative electric potentials can be found in the Moon base landscape (Figure 4f) because there is a cavity at two sides of the landscape into which solar wind protons cannot easily enter

but electrons can. Furthermore, inside the cavity, even the horizontal surface does not emit photoelectrons because it is in the shadow.

The 2-D electric potential structures result in different dust density profiles above the landscapes, as can be seen in Figure 5. The homogeneously emitted dust forms various large-scale density minimum and maximum regions. Density enhancements also form narrow density stripes that are associated with the corners in the landscape features, which separate positively charged surface regions from the negatively charged surface regions (see electric potential in Figure 4). The dust densities shown in Figure 5 mimic the situation of continuous interplanetary dust bombardment or when there is a meteoric shower, which results in the emission of dust particles from a wide surface region. The maximum density regions in the figures are related to the turning of the upward moving velocity to the downward moving velocity. Near the turning point the velocity of dust particles becomes small and, consequently, their density becomes high.

Figure 6, instead, shows dust densities at cases where there is a localized dust emission on the surface. This situation may mimic dust emission caused by robotic or human activity on the lunar surface or dust emission caused by a single micrometeoroid impact. Four dust emission positions on the surface were analyzed: (1) a point at $y = -25$ m far away from the nonplanar surface region, (2) a point at $y = -11$ m where the landscape feature starts, (3) a point at $y = -6$ m which is located on the side of the landscape, and (4) a point at $y = -0.25$ m which is close to the center of the landscape. Figure 6 indicates that a localized dust emission results in highly different dust distributions depending on the landscape shape and on where the source is located with respect to the landscape. In some cases a dust "fan" is formed (see, e.g., $y = -11$ m in the antipyramid case), while in some other cases a relatively narrow, vertically tilted dust jet (see, e.g., $y = -6$ m in the crater case) can be seen. In several cases there is a local density maximum above the source but not always because of the nonhomogeneous horizontal electric fields accelerating the dust particles horizontally, i.e., away from the vertical to the source (see, e.g., $y = -11$ m in the crater case).

3.3. Discussion

This paper describes details of the new electrostatic PIC code developed to study plasmas and electric fields above different lunar landscapes. The applicability of the PIC code is not restricted to the lunar surface, and it can be used equally well to study the near-surface plasma of an asteroid, Mercury, moons of giant planets, or a nonactive or weak comet.

The model has been found to be robust and flexible to study various landscapes and physical properties of the landscape. This is accomplished by developing suitable boundary conditions for fields and particles and by introducing a method (the material index) to describe landscape features and properties of the surface. In this paper 1-D and 2-D versions were used to study six different landscape features. The model can also be used in 3-D, as implied by preliminary low-resolution test runs (figures not shown) but a good-resolution 3-D case requires substantially more computing resources than 1-D or 2-D cases.

Analysis of the six landscapes showed, that the near surface electric field is controlled by the landscape. For a comparison, variations of the electric potential from point to point near a landscape can easily exceed the variations that can be seen at different SZA values on flat surface cases (e.g., cf. Figures 2b and 3b). The 2-D electric potential distributions in turn was found to significantly affect dust density profiles both in the case when there is a dust emission from the whole surface and when there is a localized dust source. A practical implication of these results is that the landscape morphology has to be taken into account when an appropriate site for a human or robotic action on the surface is planned.

In the future more detailed studies for the near-surface physics can be made for the HYBes by including more charged particles, using non-Maxwellian velocity distribution function, analyzing various solar illumination conditions and including plasma-dust interactions. For example, the photoelectron and solar wind velocity distribution functions can be non-Maxwellian in the HYBes model. In this paper we assume that all initial velocity distributions are 3-D Maxwellian distributions to make the result comparable with previous published Debye sheath PIC simulations [*Poppe and Horányi*, 2010; *Kallio et al.*, 2012]. In a more rigorous modeling one should take into account the fact that the energy spectra of the solar radiation vary with time depending on the solar activity and that the photoelectron yield is depending on the solar optical spectrum. For example, it has been shown that extreme solar flare conditions can increase photoelectron emission several fold [*Sternovsky et al.*, 2008]. The energy distribution of electrons depends also strongly on the chemical composition of the material from which the photoelectrons are emitted, such as its oxidation

state [*Grard and Tunaley*, 1971]. In addition, a Maxwellian velocity distribution function is only the first-order approximation for the solar wind protons and electrons. It should also be noted that lunar surface emits also secondary ions and electrons, which also can be included into the HYBes in a manner similar to photoelectrons.

Other simplification in the analyzed situation is that dust particles were modeled as charged particles which do not contribute self-consistently to the total charge density of the plasma from which the electric potential is derived. The charge and the mass of the dust particle are also assumed to be unchanged; however, the charge may change due to photoelectron emission. In the present study dust particles are modeled as test particles and there is no feedback from charged dust particles to the electric potential and vice versa. It has, however, been argued that electrons stripped from dust particles, i.e., the so-called "dust electrons," may be a dominant source of electrons below 100 km [*Stubbs et al.*, 2011]. Modeling the dust in the HYBes would require determining the flux of dust particles released from the surface; however, the emission rate is still unknown. The dust densities presented in Figures 3, 5, and 6 can, therefore, be interpreted for the case where the charge density associated with dust particles is so small that they do not affect the electric potential within the Debye layer. Such a fully self-consistent dusty plasma simulation is, however, challenging because the time scale in the PIC simulation, determined by the electron plasma frequency ($\sim 9\sqrt{n(e^-)}$ kHz, where the electron density is given in cm^{-3}), is much smaller than the typical time of residence of a dust particle in the simulation box.

Note that the time for a charged particle reaching its equilibrium charge in a plasma can be very large compared with the time for which a dust particle stays above the surface. The charging time by plasma electrons has been approximated to be of the order of $4.1 \times 10^3 (T(e^-)\ [\mathrm{eV}]/50)^{1/2}/(r\ [\mu\mathrm{m}]\ n_{sw}\ [\mathrm{cm}^{-3}]/5)$ s, where r is the radius of a spherical dust particle [*Nitter et al.*, 1992]. For example, in the case analyzed bin the paper ($n_{sw} = 10$ cm^{-3}, $k_b T(e^-) = 10.5$ eV) the charging times for 0.01, 0.1, 1, and 10 μm dust particles would be about 94,000 s (26 h), 9400 s (2.6 h), 940 s (16 min), 94 s (1.6 min), respectively. These times are much longer that it takes for a surface-emitting photoelectron to reach an equilibrium charging. For example, the running time of the 2-D PIC simulations was 1 ms. However, a dust particle on the surface bis already in a charge equilibrium state and, therefore, the time development of the charge of the dust particle is anticipated to be controlled by the properties of the ambient plasma. These charging times are substantially longer than the time it takes for HYBes to reach a stationary state in the cases analyzed in this paper, suggesting that the assumption of an unchanged electric charge for the dust particles is a good first-order approximation when dealing with dust particles of ~ 0.05 μm radius.

An additional simplification in the analyzed cases was that the magnetic field was assumed to be zero, i.e., the magnetic fields associated with the IMF or the Earth's magnetosphere were missing. In addition the Moon exhibits localized magnetic anomalies [e.g., *Lin et al.*, 1998]. The new HYBes model can also include time-independent, spatially variable magnetic fields, including the IMF or the lunar magnetic anomalies. Recently, 3-D properties of plasmas and fields were studied with a hybrid model [*Jarvinen et al.*, 2014] that enabled separation of the flow of ions and electrons but which assumed a quasi-neutral plasma, that is, the density of electrons is equal the density of protons. The hybrid model assumed a massless electron fluid and, consequently, did not include fast electron plasma oscillations in contrast with a full PIC simulation, which requires a small simulation time step and long computation times. In the future, embedding the small spatial domain PIC simulation model inside a global or meso-spatial-scale model may increase the applicability of a 2-D or a 3-D PIC simulation toward the study of larger spatial structures with reasonable computer resources (see *Kallio et al.* [2012] for the discussion of different spatial scales in the lunar plasma environment models].

3.4. Summary

A new 1-D/2-D/3-D electrostatic full kinetic particle-in-cell model, HYBes, has been developed to study space plasma associated with the direct plasma-surface interaction. The model enables the analysis of the properties of ions, electrons, and the electric field above various nonplanar surfaces. Simulation runs made for different 2-D landscape features indicate that the detailed landscape morphology strongly affects the electric field above the surface, in agreement with suggestions from previous PIC models. Different 2-D electric fields were also found to result in highly different 2-D dust distributions above the surface. These results show that the morphology of the landscape is critical to our understanding of the lunar near-surface

plasma, and field and dust environments and that a 2-D or a 3-D PIC model is required to simulate these near-surface regions.

Appendix A: Electric Potential on the Front and Back Walls

The minimum requirement for the HYBes model is that it gives the electric potential in a planar case, that is, when parameters vary only with the altitude: $\rho_q = \rho_q(x)$, $\phi = \phi(x)$, $\mathbf{E} = (E_x(x), 0, 0)$. The HYBes assumes that the charge density outside of the simulation box is zero, that is, a quasi-neutrality outside of the simulation region. The electric field at the x_{min} and x_{max} faces can be obtained from Gauss's law by integration along the x axis:

$$\nabla \cdot \mathbf{E} = -\frac{\rho_q}{\epsilon_0} \Longrightarrow E_x(x_{max}) - E_x(x_{min}) = -\frac{Q}{dl^2\epsilon_0} \tag{A1}$$

where dl^2 $(= (y_{max} - y_{min})(z_{max} - z_{min}))$ is the area of faces at x_{min} and x_{max}. Q is the total electric charge in the simulation box, which contains the electric charge above the surface (Q_{space}) and the electric charge on the lunar surface (Q_{surf}): $Q = Q_{space} + Q_{surf}$. The 1-D density profile represents the real 3-D space collection of infinite large electric charge planes where every plane of a width dx has a surface charge density of $\rho_q(x)$dx. Such surface charge results in a constant electric field on both sides of the plane such that the direction of the electric field on the opposite side of the plane is opposite. Therefore, at the top and bottom faces $E_x(x_{max}) = -E_x(x_{min})$ applies. Combining of this to equation (A1) gives

$$E_x(x_{max}) = -E_x(x_{min}) = -\frac{Q}{2\epsilon_0} \tag{A2}$$

In the full 2-D or 3-D cases the result of the volume integration of equation (A2) can be written as follows:

$$< E_x(x_{max}) > dl^2 - < E_x(x_{min}) > dl^2 = -\frac{Q}{\epsilon_0} \tag{A3}$$

where $< E_x(x_{max}) >$ and $< E_x(x_{min}) >$ are the average electric field on the $x = x_{max}$ and on the $x = x_{min}$ planes, respectively.

The HYBes simulation assumes that there is no electric field or charge density outside of the simulation box, that is,

$$E_x = 0; \rho_q = 0. \tag{A4}$$

According to Gauss's law, the required zero electric flux through the simulation box implies that the total charge within the box is zero ($Q = 0$). Therefore, equation (A3) gets the form

$$< E_x(x_{max}) > = - < E_x(x_{min}) > . \tag{A5}$$

The HYBes uses equation (A5) and assumes that the electric field is constant on the x_{max} and x_{min} faces, that is,

$$\begin{aligned} E_x(x_{max}, y, z) &= < E_x(x_{max}) > \\ E_x(x_{min}, y, z) &= < E_x(x_{min}) > \end{aligned} \tag{A6}$$

where

$$< E_x(x_{max}) > = - < E_x(x_{min}) > = -\frac{Q}{2\epsilon_0 dl^2} \tag{A7}$$

It should be noted that equation (A6) becomes more and more accurate the farther away the x faces are from the region where Q is nonzero, that is, the larger the simulation box is in the x direction.

Equations (A6) and (A7) form the boundary conditions for the fields at the upper and lower faces, and these are used for the boundary conditions for the electric potential as follows:

$$\begin{aligned} \phi(0) &= \phi(1) - \frac{Q}{2dl\epsilon_0}, \\ \phi(N_x - 1) &= \phi(N_x - 2) - \frac{Q}{2dl\epsilon_0}. \end{aligned} \tag{A8}$$

Appendix B: Density Regulator Method

The most critical boundary condition in the HYBes controls how the solar wind particles are injected into the simulation box. Before the density regulator, DR, method was implemented into HYBes, various other boundary conditions were tested that all resulted in some unwanted effects, such as short- or long-wavelength nonvanishing fluctuations or a plasma sheath near the front wall. The important feature in the DR method is that it does not result in artificial plasma or field regions near the simulation boundaries and, therefore, the result within the full simulation box can be used.

It is important to realize why the front wall boundary condition is challenging to see the rationale behind the developed DR. The HYBes simulation tries to reach a stationary solution. Conservation of the electric charge states that

$$\frac{\mathrm{d}\rho_q}{\mathrm{d}t} + \nabla \cdot \mathbf{j} = 0 \tag{B1}$$

where ρ_q and j are the total charge density and the electric current density, respectively. Note that equation (B1) is valid even when new charged particles are generated inside the simulation box because new charged particles, such as photoelectrons and corresponding positively charged ions on the surface, originate from an atom or a molecule. Therefore, the amounts of negatively and positively charged particles are equal and, consequently, they do not affect the total charge density ρ_q.

Integration of equation (B1) over the volume of the simulation box states that in a stationary case the total electric current into the simulation box should be zero. Because periodic boundary conditions are used in the y and z directions and because particles are not moving through the bottom boundary, the total electric current J_{tot} (A) through the upper wall should be zero:

$$J_{\mathrm{tot}} = \sum_k J_k = J_{x_{\mathrm{max}}}(e^-_{\mathrm{sw}}) + J_{x_{\mathrm{max}}}(H^+_{\mathrm{sw}}) + J_{x_{\mathrm{max}}}(P^{\pm}_{\mathrm{Moon}}) = 0 \tag{B2}$$

Here $J_x(e^-_{\mathrm{sw}})$ and $J_x(H^+_{\mathrm{sw}})$ are the total electric current through the upper wall associated with the solar wind electrons and protons, respectively. The total electric current $J_x(P^{\pm}_{\mathrm{Moon}})$ is associated with all charged particles originating from the surface, $P^{\pm}_{\mathrm{Moon}}$, such as the photoelectrons, secondary electrons and ions, and charged dust particles.

Another boundary condition is that we assume quasi-neutrality near the front wall, that is,

$$e \cdot n(e^-_{\mathrm{sw}}) = e \cdot n(H^+_{sw}) + q_{\pm} \cdot n(P^{\pm}_{\mathrm{Moon}}) \tag{B3}$$

where e and $q_{\pm}$ are the positive unit charge and the electric charge of the particle $P^{\pm}_{\mathrm{Moon}}$. In the current simulation $P^{\pm}_{\mathrm{Moon}}$ includes only photoelectrons.

It is instructive to consider the consequences and challenges of particle boundary conditions in equations (B2) and (B3) before we introduce the DR. Let us then assume a two-charged-particle population plasma formed by the solar wind electrons and protons. Assume now a typical situation in the solar wind where the bulk velocity of protons, $U_{\mathrm{sw}}(H^+)$, is much larger than their thermal velocity and that, therefore, all protons at the front wall move toward the surface. Assume also a typical situation in the solar wind that the bulk velocity of electrons in the undisturbed solar wind, $U_{\mathrm{sw}}(e^-)$, is much smaller than their thermal velocity. This means that if the undisturbed velocity distribution function of electrons is $f_e(v)$, in the simulation only downward moving electrons, $v_x < 0$, move into the simulation box at the front wall.

The full velocity distribution at the front wall instead is a superposition of downward moving electrons and upward moving electrons ($v_x > 0$), which are reflected back from the electric potential (i.e., which move out of the simulation box) with a velocity distribution function of $f^{\mathrm{ref}}_e(v)$. Note that the conservation of energy states that the speed of a reflected electron is equal to the speed of the initial electron but the direction of the velocity is opposite. Therefore, the total velocity distribution of electrons at the front wall, $f^{\mathrm{tot}}_e(v)$, is the superposition of the initial (half) Maxwellian velocity distribution and the reflected electrons formed by those slow SW electrons which had their direction of velocity changed:

$$f^{\mathrm{tot}}_e(v) = f_e(v) + f^{\mathrm{ref}}_e(v) \tag{B4}$$

Therefore, there is a reflection velocity, v_r, and electrons with a velocity smaller than v_r become reflected back to the front wall. Formally this can be written as

$$f_e^{\mathrm{ref}}(v) = f_e(-v), \;\; 0 < v < v_r$$
$$f_e^{\mathrm{ref}}(v) = 0, \;\; v > v_r \tag{B5}$$

The value of v_r depends on the maximum local potential minimum, ϕ_{min}, from the law of conservation of energy is

$$\frac{1}{2} m_e v_r^2 = e\phi_{\mathrm{min}} \tag{B6}$$

when the gravitation is neglected. In a more rigorous analysis for a small potential drop and a high gravity object, also the gravitation has to be taken into account.

The total electron distribution function f_e^{tot} can be derived from the boundary conditions, equations (B2) and (B3), which in the two-population solar wind plasma are

$$-en_e U_x(e^-) + en(H^+)U_x(H^+) = 0 \tag{B7}$$

$$n_e = n(H^+) \tag{B8}$$

Combining the equations implies that the bulk velocity of electrons and ions are equal:

$$U_x(e^-) = U_x(H^+) \tag{B9}$$

Equation (B9) states that in the quasi-neutral solar wind, electrons and protons have the same bulk speed. Within the simulation box the potential drop is of the order of a few eV for a typical solar wind plasma [see, e.g., *Poppe and Horányi*, 2010]. Therefore, the velocity distribution of the solar wind protons can be approximated to be unchanged within the simulation box and, consequently, the bulk velocity of the protons to be equal the velocity of the solar wind:

$$U_x(H^+) = U_{\mathrm{sw}}(H^+) \tag{B10}$$

Equations (B8) and (B3) give us the needed condition for the velocity distribution of electrons:

$$U_x(e^-) = U_{\mathrm{sw}}(H^+) = \mathrm{const.} \tag{B11}$$

Finally, equation (B11) can be used to derive the reflection velocity (v_r) in equation (B4) analytically or numerically in the following steps: (1) choose a small nonzero value for v_r, (2) derive f_e^{ref} from equation (B5), (3) derive f_e^{tot} from equation (B4), (4) calculate $U_x(e^-)$ at the front wall. If equation (B11) is not fulfilled then increase the value v_r until it is fulfilled. Note that v_r can always be found because in the solar wind $U_x(e^-) = U_{\mathrm{sw}}(H^+) < 0$, but f_e includes only downward moving electrons. Therefore, $U_x(e^-)$ associated with f_e is smaller than $U_{\mathrm{sw}}(H^+)$, and its value can be increased up to $U_{\mathrm{sw}}(H^+)$. The reflected electrons increase the negative $U(e^-)_x$ until it is equal to $U_{\mathrm{sw}}(H^+)$. Note also that when v_r is known, one can also calculate the minimum potential drop for equation (B6). At this stage only the information about the shape of the velocity distribution function f_e is used. The normalization of f_e can be obtained from the quasi-neutrality condition equation (B4), noting that a very good approximation for the $n(H^+)$ is the undisturbed density of solar wind protons.

The importance of the boundary condition algorithm sketched above is that it makes it understandable why one can always find a solution which fulfills both the quasi-neutrality and where the electric current inside the simulation box is zero. It should, however, be noted that above we assumed that the velocity distribution of protons was unchanged by the electric potential and, therefore, there were only two free parameters (v_r and a normalization constant for $f_e^{\mathrm{tot}}(v)$) whose value could be determined by two scalar equations describing the boundary conditions (equations (B7) and (B8)). In reality the situation is more complicated because there are also charged particles of lunar origin and we do not know beforehand how large is their contribution to the total electric charge and the electric current at the front face (see equations (B2) and (B3)). The velocity distribution function of protons can be changed within the Debye sheath. Therefore, the boundary conditions for particles cannot be derived in a general case with the aforementioned algorithm without making the actual self-consistent simulation.

In the HYBes model a new particle BC was created where it is linked to the field BC by modifying automatically the density of the undisturbed solar wind distribution function f_e^{tot}. The density modification affects the electric potential and the number of reflected SW electrons. The automatic density modification by the DR is continued in the simulation run until the electric field near the solar wind face is zero, that is, until the electric potential is constant near the solar wind. The constant electric potential also implies that the plasma is quasi-neutral in that region. By this automatic regulation of the solar wind electron flux, a stationary solution is obtained that fulfills simultaneously the requirements of quasi-neutrality and the zero electric current through the front wall.

Technically, the DR is implemented as follows: it increases or decreases the density of injected solar wind electrons if the total charge within the simulation box is positive or negative, respectively. In such a way the total electric charge within the simulation box becomes closer to zero and, consequently, the electric field near the front wall closer to zero. In such a way the number of backscattered solar wind electrons is changed indirectly. The two control parameters in the DR are the time interval during which the total electric charge inside the simulation box was derived, Δt_{DR}, and the density change factor, Δn_{DR}, which determines how much the density of the solar wind electrons was increased or decreased at every Δt_{DR}. In the presented runs DR was started after 1 ms of the beginning of the simulation, $\Delta t_{\mathrm{DR}} = 6.25 \cdot 10^{-6}$ s and Δn_{DR} was 0.5%. In general, values of Δt_{DR} and Δn_{DR} are expected to depend on the simulated case, such as the size of the simulation box and the input parameters.

Acknowledgments

S.D. and E.K. thank Cyril Simon Wedlund (Aalto University, Finland) for the careful reading of the manuscript and helpful comments and suggestions. P.W. acknowledges financial support by the Swiss National Science Foundation and S.D. acknowledges Academy of Finland (251573). E.K. acknowledges ESA GSP program project DPEM, Dusty plasma environments: near-surface characterization and modeling (ESA ITT, AO-1-6696/11/NL/CO) for the financial support for the work. E.K. also thanks A.R. Poppe for the useful discussions about challenges of PIC simulations. The data presented in this paper are available upon request from the authors (S.D. and E.K.).

Michael Balikhin thanks Rejean Grard and another reviewer for their assistance in evaluating this paper.

References

Criswell, D. R. (1973), Horizon-glow and the motion of lunar dust, in *Photon and Particle Interactions With Surfaces in Space in Proceedings of the 6th Eslab Symposium, Held at Noordwijk, the Netherlands, 26–29 September, 1972, Series: Astrophysics and Space Science Library*, vol. 37, pp. 545–556, Springer, Netherlands.

Dyadechkin, S. A., E. Kallio, and R. Jarvinen (2013), A new 3-D spherical hybrid model for solar wind interaction studies, *J. Geophys. Res. Space Physics*, *118*, 5157–5168, doi:10.1002/jgra.50497.

Farrell, W. M., J. S. Halekas, T. J. Stubbs, G. T. Delory, R. M. Killen, R. E. Hartle, and M. R. Collier (2011), Regarding the possible generation of a lunar nightside exo-ionosphere, *Icarus*, *216*, 169–172.

Grard, R. J. L., and J. K. E. Tunaley (1971), Photoelectron sheath near planar probe in interplanetary space, *J. Geophys. Res.*, *76*(10), 2498–2505.

Hartzell, C. M., and D. J. Scheeres (2011), The role of cohesive forces in particle launching on the Moon and asteroids, *Planet. Space Sci.*, *59*, 1758–1768.

Hockney, R., and J. Eastwood (1988), *Computer Simulation Using Particles*, Adam Hilger, Bristol and Philadelphia, Bristol, Great Britain.

Jardin, S. (2010), *Computational Methods in Plasma Physics, Chapman and Hall/CRC Computational Science Series*, CRC Pres, Taylor and Francis Group, New York.

Jarvinen, R., M. Alho, E. Kallio, P. Wurz, S. Barabash, and Y. Futaana (2014), On vertical electric fields at lunar magnetic anomalies, *Geophys. Res. Lett.*, *41*, 2243–2249, doi:10.1002/2014GL059788.

Kallio, E., et al. (2012), Kinetic simulations of finite gyroradius effects in the lunar plasma environment on global, meso, and microscales, *Planet. Space Sci.*, *74*, 146–155, doi:10.1016/j.pss.2012.09.012.

Lin, R. P., D. L. Mitchell, D. W. Curtis, K. A. Anderson, C. W. Carlson, J. McFadden, M. H. Acuña, L. L. Hood, and A. Binder (1998), Lunar surface magnetic fields and their interaction with the solar wind: Results from lunar prospector, *Science*, *281*(5382), 1480–1484, doi:10.1126/science.281.5382.1480.

Nitter, T., O. Havnes, and F. Melandsö (1992), Dynamics of dust in a plasma sheath and injection of dust into the plasma sheath above Moon and asteroidal surfaces, *Earth Moon Planets*, *56*, 7–34.

Nitter, T., O. Havnes, and F. Melandsö (1998), Levitation and dynamics of charged dust in the photoelectron sheath above surface in space, *J. Geophys. Res.*, *103*(A4), 6605–6620.

Poppe, A. R. (2011), Modeling, theoretical and observational studies of the lunar photoelectron sheath, PhD thesis, Univ. of Colo., Boulder, Colo.

Poppe, A., and M. Horányi (2010), Simulations of the photoelectron sheath and dust levitation on the lunar surface, *J. Geophys. Res.*, *115*, A08106, doi:10.1029/2010JA015286.

Poppe, A., J. S. Halekas, and M. Horányi (2011), Negative potentials above the day-side lunar surface in the terrestrial plasma sheet: Evidence of non-monotonic potentials, *Geophys. Res. Lett.*, *38*, L02103, doi:10.1029/2010GL046119.

Poppe, A., J. S. Halekas, G. T. Delory, W. M. Farrell, V. Angelopoulos, J. P. McFadden, J. W. Bonnell, and R. E. Ergun (2012a), A comparison of ARTEMIS observations and particle-in-cell modeling of the lunar photoelectron sheath in the terrestrial magnetotail, *Geophys. Res. Lett.*, *39*, L01102, doi:10.1029/2011GL050321.

Poppe, A., M. Piquette, A. Likhanskii, and M. Horányi (2012b), The effect of surface topography on the lunar photoelectron sheath and electrostatic dust transport, *Icarus*, *221*, 135–146.

Rennilson, J. J., and D. R. Criswell (1974), Surveyor observations of lunar horizon glow, *The Moon*, *10*, 121–142.

Sternovsky, Z., P. Chamberlin, M. Horányi, S. Robertson, and X. Wang (2008), Variability of the lunar photoelectron sheath and dust mobility due to solar activity, *J. Geophys. Res.*, *113*, A10104, doi:10.1029/2008JA013487.

Stubbs, T. J., D. A. Glenar, W. M. Farrell, R. R. Vondrak, M. R. Collier, J. S. Halekas, and G. T. Delory (2011), On the role of dust in the lunar ionosphere, *Planet. Space Sci.*, *59*, 1659–1664.

Walker, E. H. (1973), The lunar electronosphere and implications for erosion on the Moon, in *Photon and Particle Interactions With Surfaces in Space in Proceedings of the 6th Eslab Symposium, Held at Noordwijk, the Netherlands, 26–29 September, 1972, Series: Astrophysics and Space Science Library*, vol. 37, pp. 521–546, Springer, Netherlands.

Zimmerman, M. I., W. M. Farrell, T. J. Stubbs, J. S. Halekas, and T. L. Jackson (2011), Solar wind access to lunar polar craters: Feedback between surface charging and plasma expansion, *Geophys. Res. Lett.*, *38*, L19202, doi:10.1029/2011GL048880.

Zook, H. A., and J. E. McCoy (1991), Large scale lunar horizon glow and a high altitude lunar dust exosphere, *Geophys. Res. Lett.*, *18*, 2117–2120.